Freeze-out configuration properties in the ^{197}Au + ^{197}Au reaction at 23A MeV

R. Najman,[1] R. Płaneta,[1,*] A. Sochocka,[2] F. Amorini,[3,4] L. Auditore,[5] T. Cap,[6] G. Cardella,[7] E. De Filippo,[7] E. Geraci,[4,7] A. Grzeszczuk,[8] S. Kowalski,[8] T. Kozik,[1] G. Lanzalone,[3,9] I. Lombardo,[10,11] Z. Majka,[1] N. G. Nicolis,[12] A. Pagano,[7] E. Piasecki,[13,14] S. Pirrone,[7] G. Politi,[4,7] F. Rizzo,[3,4] P. Russotto,[7] K. Siwek-Wilczyńska,[6] I. Skwira-Chalot,[6] A. Trifiro,[15] M. Trimarchi,[15] J. Wilczyński,[14,†] and W. Zipper[8]

[1]*M. Smoluchowski Institute of Physics, Jagiellonian University, Kraków, Poland*
[2]*Department of Physics, Astronomy and Applied Informatics, Jagiellonian University, Kraków, Poland*
[3]*INFN, Laboratori Nazionali del Sud, Catania, Italy*
[4]*Dipartimento di Fisica e Astronomia Università di Catania, Catania, Italy*
[5]*Dipartimento di Fisica e Scienze della Tera Università di Messina and INFN Gruppo Collegato di Messina, Italy*
[6]*Faculty of Physics, University of Warsaw, Warsaw, Poland*
[7]*INFN, Sezione di Catania, Italy*
[8]*Institute of Physics, University of Silesia, Katowice, Poland*
[9]*Università degli Studi di Enna "Kore", Enna, Italy*
[10]*Dip. di Fisica, Università di Napoli Federico II, Naples, Italy*
[11]*INFN, Sezione di Napoli, Italy*
[12]*Department of Physics, The University of Ioannina, Ioannina, Greece*
[13]*Heavy Ion Laboratory, University of Warsaw, Warsaw, Poland*
[14]*National Centre for Nuclear Research, Otwock-Świerk, Poland*
[15]*Dipartimento di Fisica Università di Messina and INFN Gruppo Collegato di Messina, Italy*

(Received 15 July 2015; published 28 December 2015)

Data from an experiment on the ^{197}Au + ^{197}Au reaction at 23A MeV are analyzed with an aim to find signatures of exotic nuclear configurations such as toroid-shaped objects. The experimental data are compared with predictions of the ETNA code, dedicated to look for such configurations, and with the quantum molecular dynamics (QMD) model. A novel criterion of selecting events possibly resulting from the formation of exotic freeze-out configurations, "the efficiency factor," is tested. Comparison between experimental data and model predictions may indicate the formation of flat and/or toroidal nuclear systems.

DOI: 10.1103/PhysRevC.92.064614 PACS number(s): 25.70.Gh, 25.70.Pq

I. INTRODUCTION

The search for exotic nuclear configurations was inspired by Wheeler [1]. His idea was investigated by many authors who studied the stability of exotic nuclear shapes (see, e.g., [2–4]). Theoretical investigations have shown that very exotic extra-superheavy nuclei can be reached only if noncompact shapes are taken into account. Calculations for bubble structures showed that such nuclei can be stable for $Z > 240$ and $N > 500$ (see, e.g., [5–7]). Recently it was found that for nuclei with $Z > 140$ the global energy minimum corresponds to toroidal shapes [8,9]. In contrast to bubble nuclei, the synthesis of toroidal nuclei is experimentally available in collisions between stable isotopes.

To address this issue, simulations were performed for Au + Au collisions in a wide range of incident energies using the BUU code [10,11]. These calculations indicate that the threshold energy for the formation of toroidal nuclear shapes is located around 23A MeV.

Also, improved quantum molecular dynamics (QMD) model calculations performed for U + U collisions have shown a possible formation of toroidal freeze-out configurations above a specific collision energy for this heavy system [12]. Such toroidal-shape complexes can be also created in macroscale in binary droplet collisions above some threshold velocity [13].

A number of observables were suggested as the signatures of noncompact freeze-out configurations. These were the following:

(1) Larger number of intermediate mass fragments should be observed than would be expected for the decay of a compact object.
(2) Enhanced similarity in the charge and size of the fragments should also be observed.
(3) Suppressed sphericity in the emission of fragments should be visible.

The simulations of decay processes of different breakup configurations using the ETNA code were performed to study the ability of the CHIMERA detector [14,15] for recognition of noncompact configurations. Analysis of different observables has shown that a quantity named "the efficiency factor" of events with five heavy fragments can be used as a criterion for selecting events possibly resulting from formation of toroidal configurations [16,17].

The CHIMERA Collaboration has carried out an experiment on the ^{197}Au + ^{197}Au reaction at 23A MeV beam energy, focused on two independent goals: first on the

*roman.planeta@uj.edu.pl
†Deceased.

extension of the earlier study at lower energy of 15A MeV, in which a new reaction mechanism of violent breakup of the nonfusing ^{197}Au + ^{197}Au system into three and/or four massive fragments was observed [18–20]; and second, on the search of exotic nuclear configurations such as toroidal shapes. Some preliminary results of the former project have been published in [21].

In this work we report results of our analysis focused on the question of exotic configurations involving the breakup of the ^{197}Au + ^{197}Au system into five or more fragments. The experimental data are compared with model predictions. Conclusions regarding the shape of the freeze-out configuration are drawn.

This paper is organized as follows. In Sec. II we present the experiment and data calibration procedures. General characteristics of experimental data are shown in Sec. II. The dedicated observables are discussed in Sec. IV. The conclusions are presented in Sec. V.

II. EXPERIMENT AND DATA CALIBRATION PROCEDURE

The experiment for the ^{197}Au + ^{197}Au reaction at 23A MeV was performed at the INFN-LNS Superconducting Cyclotron of Catania. During the experiment two gold targets were used: 164 and 396 μg/cm^2. The thinner target was used in calibration measurements and the thicker one in the production runs. Reaction products were detected with the CHIMERA multidetector [14,15] that consists of 1192 telescopes arranged in 35 rings in full 2π azimuthal symmetry around the beam axis, covering the polar angle between 1° and 176°. A single detection cell consists of a planar n-type silicon detector ($\cong$300 μm thickness) followed by a Cs(Tl) scintilator of thickness varing from 12 cm at forward angles to 3 cm at backward angles.

The collected data were calibrated using a set of dedicated programs developed at INFN-LNS. Energy calibration of Si detectors was performed using ion beams, delivered by both the tandem accelerator and the cyclotron. Data for the following systems were used: (i) the elastic scattering data for ^{16}O +Au at 60 and 80 MeV, ^{58}Ni + Au at 142 MeV, and Au + Au at 170 MeV and 23A MeV; (ii) the recoil peak for Au + ^{12}C at 170 MeV; and (ii) fission fragments from Au + ^{12}C reaction at 23A MeV. Unlike in the analysis of ternary breakup reactions [21] in which the pulse-height defect was calculated with the formula of Ref. [22], in the present analysis the pulse-height defect in silicon detectors was calculated using the same procedure as described in Ref. [23].

In order to identify fragments two methods were applied: (i) the ΔE-E technique for fragments punching through the silicon detectors; (ii) the time of flight (TOF) method for the class of fragments stopped in Si detectors. In Fig. 1 (upper part) an example of the ΔE-E plot is shown for a detector belonging to the third internal ring, at a polar angle $\theta = 5.2°$. The Z distribution of fragments identified by the ΔE-E method for the same detector is presented also in Fig. 1 (bottom panel). We can see that in the Z spectrum a good charge identification can be observed up to $Z = 42$. At this angular range one observes a broad maximum of the charge distribution located at charges $Z = 30$–40 corresponding to Au fission

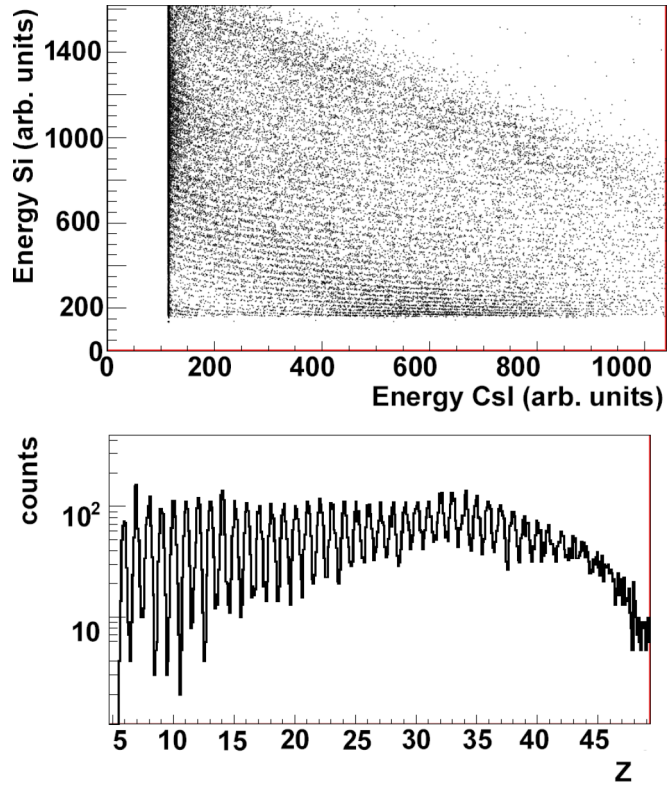

FIG. 1. (Color online) ΔE-E spectrum (upper panel) and the corresponding Z spectrum (bottom panel) for fragments detected in telescope placed at $\theta = 5.2°$ for the Au + Au reaction at 23A MeV.

fragments. One observes also a substantial contribution of lighter fragments. In order to estimate a missing information on mass of the fragments identified in charge by ΔE-E method, the EPAX formula [24–26] was used.

The mass of fragments stopped in Si detector is determined by TOF method. The start signal was given by a 30% constant-fraction discriminator acting on the time signal generated by the silicon detector, while the stop signal was given by a delayed reference signal delivered by cyclotron. Examples of ΔE-TOF spectra are presented in Fig. 2. In this case mass values are calculated using the formula

$$m = 2E(t_0 - t)^2/R^2, \quad (1)$$

where R is the distance between the target and a given detector and t_0 is a time offset of the measured time t.

A crucial problem in the calibration of TOF measurements for the CHIMERA multidetector is evaluation of the t_0 offset that must be determined for each detector individually. Moreover, t_0 depends on mass, charge, and kinetic energy of the detected fragment. The t_0 values for well identified light fragments and Au-like nuclei fragments located at the left-hand edge of the ΔE-TOF distribution (see Fig. 2) are presented by color symbols in Fig. 3. For relatively light fragments, a well tested parametrization of t_0 for CHIMERA detectors was proposed [27]. To calibrate t_0 for medium and heavy fragments in ^{197}Au + ^{197}Au experiments, a new calibration method based on a functional dependence of t_0 on mass, charge, and pulse-height-defect dependent kinetic energy was

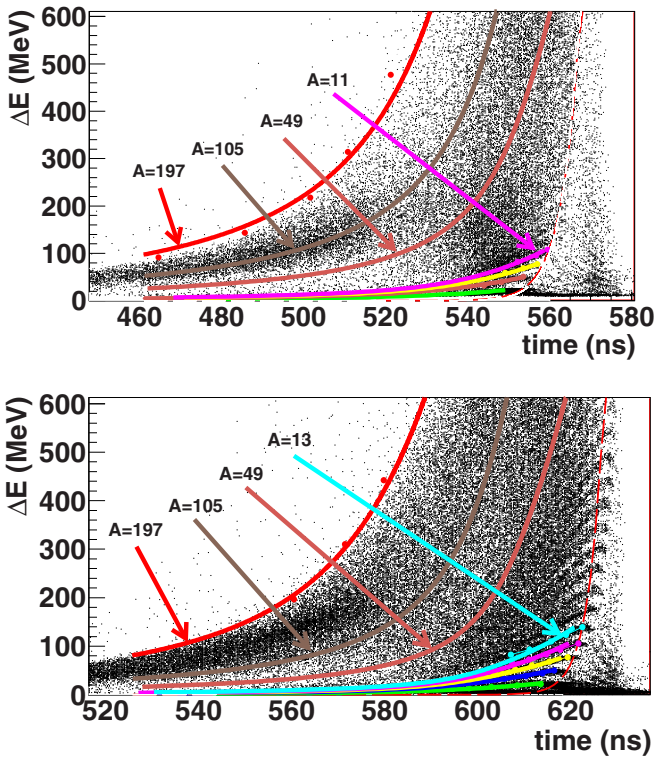

FIG. 2. (Color online) The ΔE-TOF distributions for detectors 404 (upper panel) and 653 (bottom panel) located at $\theta = 17^\circ$ and 28.5°, respectively. Lines presented in both figures correspond to positions of masses as indicated.

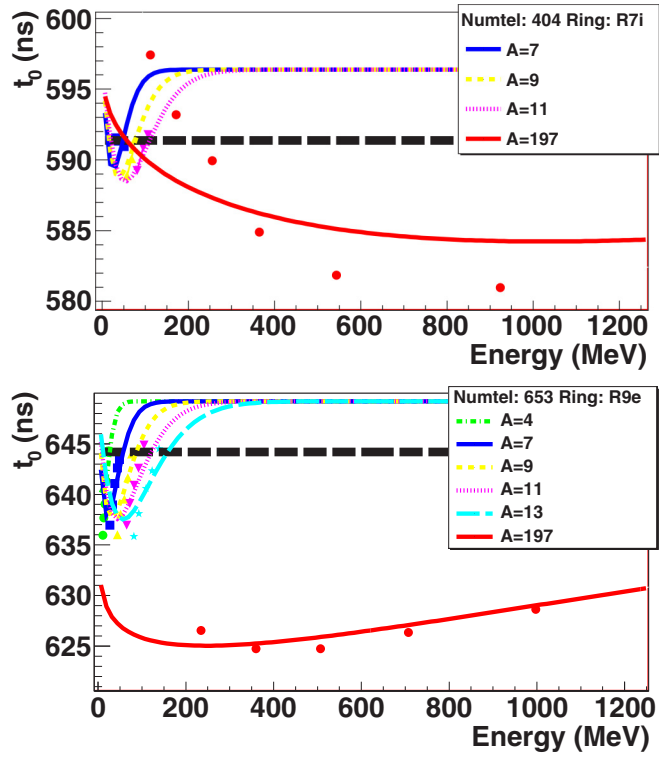

FIG. 3. (Color online) The t_0 dependence on incident energy and particle mass for telescopes 404 and 653 located at $\theta = 17^\circ$ and 28.5°, respectively. Color symbols represent the t_0 values for identified light fragments and Au-like fragments. Lines represent the fitting results using the formula. The dashed thick straight line indicates the $t_{0,\mathrm{sat}}$ value.

developed (see, e.g., [28]) and applied in analysis of the ternary breakup experiment [21].

In the present analysis we use another method of parametrization of the t_0 offset:

$$t_0 = \begin{cases} t_{0,\mathrm{sat}}, & t_{0,\mathrm{sat}} < \Delta t, \\ t_{0,\mathrm{sat}} - \Delta t, & t_{0,\mathrm{sat}} > \Delta t, \end{cases} \tag{2}$$

$$\Delta t = B - A[1 - \exp(\gamma m)]\left(\frac{E}{E_{PT}}\right)^{(\alpha - \delta m)} \times \exp\left[-\left(\frac{E + (\beta + \mu m)E_{PT}}{E_{PT}}\right)^{\epsilon}\right], \tag{3}$$

where $t_{0,\mathrm{sat}}$ is determined for particles punching through the silicon detector. The E_{PT} is the highest energy deposited by particles with mass m.

The values of the parameters A, B, α, β, γ, μ, and ϵ were determined by fitting Eq. (2) to selected points for well identified light fragments and Au-like nuclei fragments (see Fig. 3). In this procedure fragment energies were corrected for pulse-height defect, and their Z values were estimated using the EPAX formula [22–24]. Figure 3 presents the t_0 calibration lines calculated for selected mass values. The calculated positions in the ΔE-TOF distributions for some selected mass numbers are shown for two detectors in Fig. 2 as solid color lines.

In Fig. 4, two-dimensional mass versus kinetic energy distributions are shown for telescopes located at two angular regions. For the $3^\circ < \theta < 10^\circ$ region (upper panel) the distribution extends from small masses seen at low energies up to the Au elastic peak. For the $20^\circ < \theta < 29^\circ$ region (bottom panel) the particles with masses up to 200 a.m.u. are observed at relatively low kinetic energies.

III. THE GENERAL CHARACTERISTICS OF EXPERIMENTAL DATA

In Fig. 5, the two-dimensional distribution of mass versus parallel velocity of identified fragments is shown. The location of the quasielastic Au peak is visible at a mass around 200 u and velocities close to the beam velocity ($v_p = 6.67$ cm/ns). A peak corresponding to Au recoil fragments can be found at velocities close to zero. Here one can observe an underestimation of mass value for these fragments due to the imperfection of the used t_0 parametrizations (see top panel of Fig. 3). At velocities between these two limits, fragments originating from fission of the Au-like nuclei are located. One can also identify a separated region located at low masses and velocity close to the center-of-mass velocity. This region correspond to the intermediate velocity source.

For the registered events we have constructed the a presenting the dependence between the total charge of identified fragments, Z_{tot}, versus the total parallel momentum of those

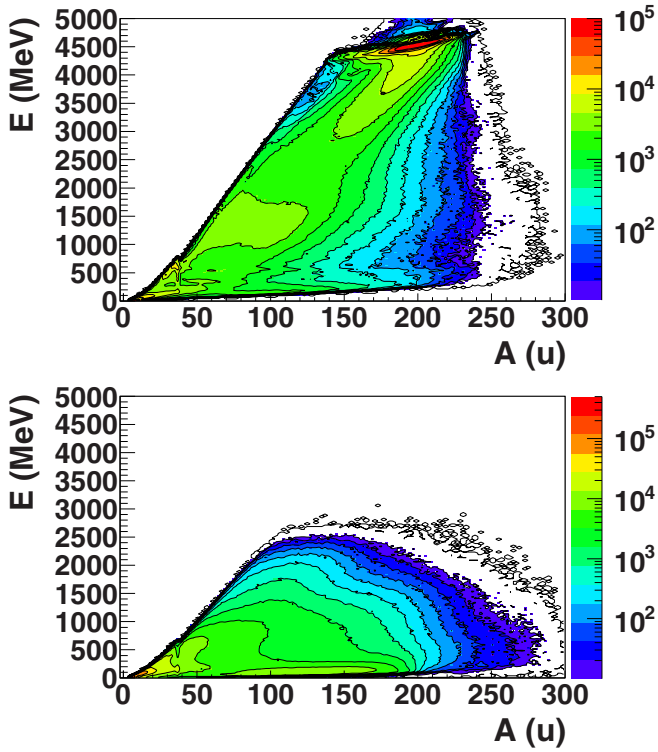

FIG. 4. (Color online) The correlation between mass and energy for fragments observed in telescopes located at $3^\circ < \theta < 10^\circ$ (upper panel) and $20^\circ < \theta < 29^\circ$ (bottom panel).

fragments normalized to the beam momentum, $p_{\parallel,\mathrm{tot}}/p_{\mathrm{proj}}$ (see Fig. 6).

One can distinguish different regions on this plot. In the region of low values of total collected charge and low parallel momentum, one observes the ridge corresponding to the badly detected events. In the region of total parallel momentum close to 1 and total collected charge close to the charge of the projectile, one observes the maximum corresponding to deep inelastic collisions where the target-like fragment remains undetected. The region where the total detected charge is close to the total charge of the system and the total parallel linear momentum is close to the linear momentum of the

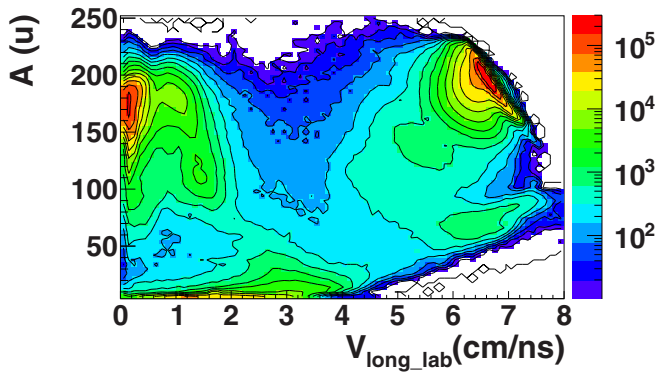

FIG. 5. (Color online) The correlation between mass of identified fragments and parallel velocity of those fragments.

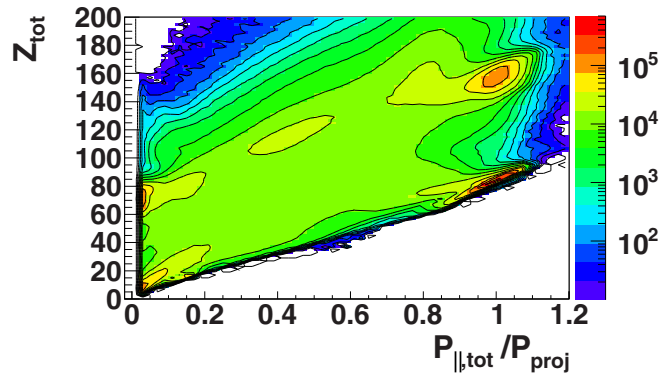

FIG. 6. (Color online) The correlation between total charge of identified fragments and total parallel momentum of those fragments normalized to the beam momentum.

projectile can be called the region of well reconstructed events. In our present analysis this region is selected by imposing the conditions $120 < Z_{\mathrm{tot}} < 180$ and $0.8 < p_{\parallel,\mathrm{tot}}/p_{\mathrm{proj}} < 1.1$. The number of events fullfiling these conditions is equal to 5.9×10^6.

For this class of well reconstructed events in the Au + Au reaction, the multiplicity distribution of fragments with charge $Z_{\mathrm{frag}} \geqslant 3$ and $Z_{\mathrm{frag}} \geqslant 10$ is presented in Fig. 7. One can notice here that the number of events with five or more fragments corresponding to above-charge thresholds is equal to about 116 000 and 6000, respectively.

IV. DATA ANALYSIS

Based on results of Ref. [18–20], in the analysis of ternary and quaternary events one expects the observation of binary deep-inelastic collisions followed by breakup of one or both primary reaction products. Results of the analysis of this particular class of reactions can be found in [21].

For the class of events with five fragments one can consider at least two mechanisms responsible for the presence of the fifth heavy fragment: (i) creation of the fragment in the interaction region (intermediate velocity source) for peripheral

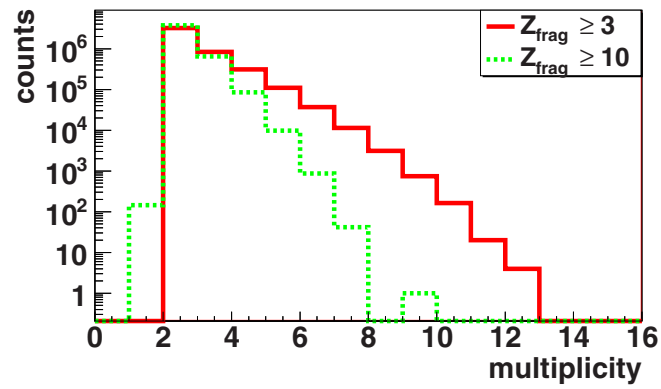

FIG. 7. (Color online) Multiplicity distributions of fragments with $Z_{\mathrm{frag}} \geqslant 3$ (red solid histogram) and $Z_{\mathrm{frag}} \geqslant 10$ (green dashed histogram).

collisions or (ii) the multifragmentation of the composite nuclear system formed in central collisions.

In order to investigate the reaction scenario responsible for events with five and more fragments, we have compared experimental data with ETNA and QMD model predicions. The ETNA model can simulate the decay of a nuclear system assuming compact and noncompact freeze-out configurations [16]. In this model three freeze-out configurations are considered: (i) ball geometry with volumes 3 and 8 times greater than normal nuclear volume V_0 (fragments uniformly distributed inside the sphere); (ii) fragments distributed on the surface of the sphere mentioned above (bubble configuration); and (iii) fragments distributed on the ring with diameter 12 and 15 fm (toroidal configuration). In this model we consider events corresponding to central collisions only (0–3 fm impact parameter range).

In order to simulate the contribution from noncentral collisions, the QMD model [29] calculations were performed in the full impact parameter range 0–12 fm. In our analysis the QMD code developed by Lukasik *et al.* [30] was used. This code takes into account (i) protons and neutrons (in standard QMD each nucleon has an effective Z/A charge); (ii) the momentum dependent Pauli potential (Skyrme + Coulomb + symmetry + surface + Pauli) is used instead of the Yukawa potential; (iii) initial nuclei in their real ground states with minimum energy (thanks to the Pauli potential) are prepared; (iv) strict angular momentum conservation in collisions is applied; (v) to simulate the Pauli blockingm in the Lukasik code the overlap of six-dimensional Gaussians is used, unlike in standard QMD where overlap of appropriate spheres in configuration and momentum space is included.

A. The shape-sensitive observables

In our analysis several observables sensitive to the freeze-out breakup configuration are investigated. First, we consider the shape of events in the momentum space [31]. The diagonalization of the momentum tensor gives three eigenvalues λ_i and three eigenvectors $\overrightarrow{e_i}$. The sphericity and coplanarity variables are defined as

$$\mathrm{sph} = 1.5(1-\lambda_1), \quad \mathrm{cop} = \frac{\sqrt{3}}{2}(\lambda_2 - \lambda_3), \tag{4}$$

where $\lambda_1 > \lambda_2 > \lambda_3$ are normalized to their sum.

In the coplanarity vs sphericity plane all events are located inside a triangle defined by points (0,0), $(\frac{3}{4}, \frac{\sqrt{3}}{4})$, and (1,0). In Fig. 8 the (sph,cop) distribution for experimental data is compared with the ETNA model predictions for Ball $8V_0$ and Toroid 15 fm freezeout decay configurations and with QMD predictions. In the case of ball geometry the maximum of the corresponding distribution is located in the center of the triangle. For the toroidal configuration the distribution is located closer to the line (0,0), $(\frac{3}{4}, \frac{\sqrt{3}}{4})$. One can see that the experimental distribution looks very similar to the QMD distribution which is dominated by the noncentral-collision contribution.

In order to reduce the noncentral contribution, we have investigated for the QMD model predictions the dependence between flow angle, θ_{flow}, and impact parameter [see Fig. 9(a)],

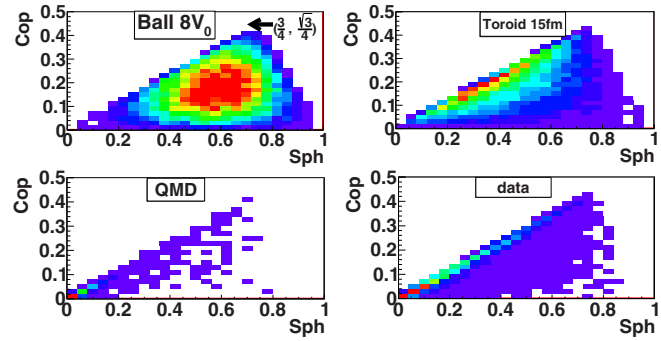

FIG. 8. (Color online) The coplanarity vs sphericity distributions for Ball $8V_0$, Toroid 15 fm, QMD, and experimental data.

where θ_{flow} is the angle between beam axis and the eigenvector $\overrightarrow{e_1}$ for the largest eigenvalue λ_1. One can see on this plot that most noncentral events are located at small θ_{flow} angles. A similar dependence is observed for experimental data between θ_{flow} and total transverse momentum, p_{trans}, used as the impact parameter estimator [see Fig. 9(c)]. We decided to reduce the contribution of noncentral events both for experimental data and model predictions by using the condition $\theta_{\mathrm{flow}} > 20^\circ$.

The δ, and Δ^2 observables as most sensitive to the shape of freeze-out configurations were selected [16]. The δ variable is related to sphericity and coplanarity variables. The δ variable measures the distance between a given point of the (sph,cop) distribution and the line defined by points (0,0), $(\frac{3}{4}, \frac{\sqrt{3}}{4})$. In Fig. 10 (left panels) the δ distributions are presented for experimental data, ETNA model predictions for considered freeze-out geometries, and QMD predictions. One can see here that the δ distribution for experimental data is similar to that corresponding QMD predictions. The biggest difference can be observed with the distribution for Ball $8V_0$ and Bubble $8V_0$ configurations.

The Δ^2 variable used in our analysis gives a measure of the event flatness in the velocity space. For each event we are establishing the plane in the velocity space. The parameters of this plane are selected in the way that the sum of squares of

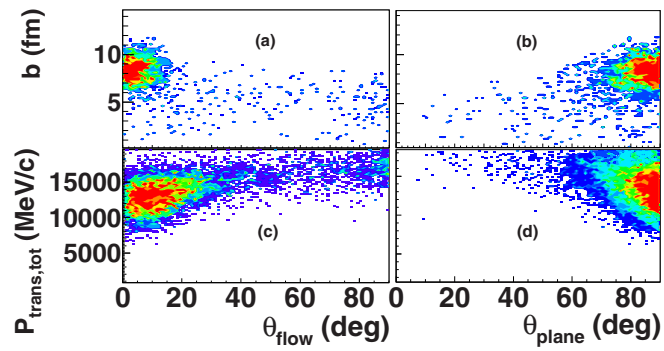

FIG. 9. (Color online) The impact parameter vs θ_{flow} dependence (a) and the impact parameter vs θ_{plane} dependence (b) for QMD model predictions. The total transverse momentum p_{trans} vs θ_{flow} dependence (c) and the total transverse momentum p_{trans} vs θ_{plane} dependence (d) for experimental data.

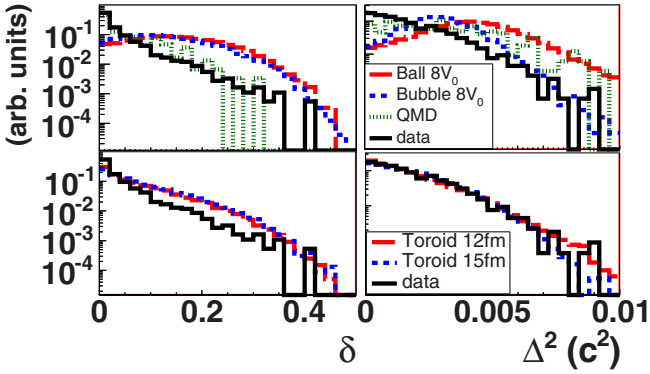

FIG. 10. (Color online) In the upper left panel the δ distributions are presented for experimental data, Ball $8V_0$, Bubble $8V_0$ freeze-out geometries, and QMD predictions. In the bottom left panel the experimental distribution is compared with predictions for Toroid 12 fm and Toroid 15 fm configurations. In the right panels the Δ^2 distributions for experimental data and model predictions are shown. All the distributions presented here are constructed using the conditions $Z_{\rm frag} \geqslant 10$ and $\theta_{\rm flow} > 20^\circ$.

distances between the plane and the endpoints $(v_{x,i}, v_{y,i}, v_{z,i})$ of velocity vectors reach the minimum value. This last quantity is called the Δ^2 parameter and is defined as

$$\Delta^2 = \min\left[\sum_{i=1}^{N_{fr}} d_i^2(A,B,C,D)\right], \tag{5}$$

where

$$d_i = \frac{|Av_{x,i} + Bv_{y,i} + Cv_{z,i} + D|}{\sqrt{A^2+B^2+C^2}}, \tag{6}$$

and parameters A, B, C, and D are the plane parameters. The plane parameters and the velocities of fragments are in velocity-of-light units.

The Δ^2 distributions are shown in Fig. 10 (right panels) for data and model predictions. One can see here that, for the Δ^2 variable, the biggest difference between the experimental distribution and model predictions is observed for the Ball $8V_0$ and Bubble $8V_0$ configurations. In contrast to that, the experimental data seem to be more consistent with the simulations assuming toroidal freeze-out configurations.

In relation to the Δ^2 parameter one can define an angle, $\theta_{\rm plane}$, between the beam direction and the vector normal to the plane defined by parameters A, B, C, and D. For events corresponding to noncentral collisions, where most of reaction products are located in the reaction plane, $\theta_{\rm plane}$ should be close to 90°. This behavior is illustrated in Fig. 9(b) for QMD model predictions, where most of noncentral events are located in the reaction plane. A similar dependence is observed for experimental data between $\theta_{\rm flow}$ and total transverse momentum, $p_{\rm trans}$, used as impact parameter estimator [see panel (d)].

The dependence between $\theta_{\rm plane}$ and $\theta_{\rm flow}$ for Ball $8V_0$, Toroid 15 fm, QMD, and experimental data is presented in Fig. 11. One observes here that for experimental data most of the events are located in the region selected by conditions $\theta_{\rm flow} < 20^\circ$

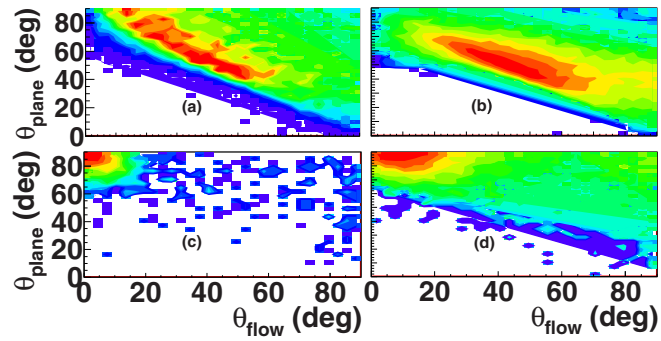

FIG. 11. (Color online) The dependence between $\theta_{\rm plane}$ and $\theta_{\rm flow}$ for Ball $8V_0$ (a), Toroid 15 fm (b), QMD (c), and experimental data (d).

and $\theta_{\rm plane} > 75^\circ$. The same behavior is observed in the case of QMD calculations. These observations indicate that such events correspond to noncentral collisions. For the Ball $8V_0$ configuration one observes the correlation between $\theta_{\rm flow}$ and $\theta_{\rm plane}$ angles. For toroidal configuration the correlation between these angles is even stronger. Most of these events are located in the region defined by conditions $\theta_{\rm flow} > 20^\circ$ and $\theta_{\rm plane} < 75^\circ$.

Following the method proposed in Ref. [16], we select events corresponding to a toroidal shape by the set of conditions

$$\Delta^2 < 0.001c^2 \quad \text{and} \quad \delta < 0.05. \tag{7}$$

As an efficiency measure of the above conditions we take the ratio of number of events fulfilling the selection conditions to the number of events with five and more heavy fragments. Hereafter, this ratio is called the efficiency factor (EF).

The results of this procedure are presented in Fig. 12 for different regions of $\theta_{\rm flow}$ and $\theta_{\rm plane}$ angles. As one can see, the EF is very low for spherical freeze-out configurations with respect to the corresponding values for toroidal configurations.

For QMD calculations the value of the efficiency factor is strongly dependent on the $\theta_{\rm plane}$ range. The condition $\theta_{\rm plane} < 75^\circ$ reduces the number of flat noncentral events mostly located in the reaction plane. For events selected additionally by the condition $\theta_{\rm flow} < 20^\circ$ the EF drops to zero.

For experimental data the value of the efficiency factor is about 50% for events located in the reaction plane ($\theta_{\rm plane} > 75^\circ$) and is reduced by factor of 2 for events perpendicular to the reaction plane. These values are weakly dependent on the $\theta_{\rm flow}$ angle range.

One observes that the values of the EF for experimental data are much larger than the corresponding predictions for QMD model. The biggest difference is observed for events located outside the reaction plane ($\theta_{\rm plane} < 75^\circ$) at small $\theta_{\rm flow}$ angles.

In order to investigate a possible formation of toroidal configurations in our analysis, we selected the region where according to ETNA predictions the toroidal configuration is most pronounced in the $\theta_{\rm flow}$ and $\theta_{\rm plane}$ plane ($\theta_{\rm plane} < 75^\circ$ and $\theta_{\rm flow} > 20^\circ$). In Table I the efficiency factor values are given for experimental data and model predictions. The efficiency factor values are shown for four threshold values of the fragment charge.

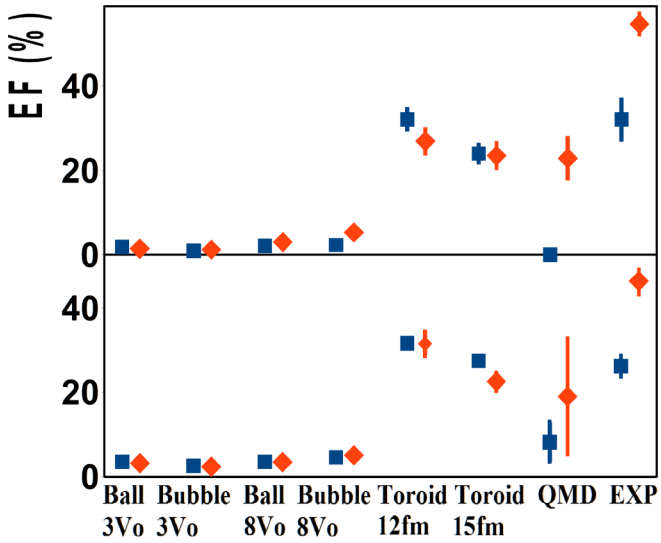

FIG. 12. (Color online) The EF values for different windows of θ_{plane} and θ_{flow}. The upper panel presents the EF values for data selected by the condition $\theta_{\text{flow}} < 20^\circ$ and the lower panel correspond to the data selected by the condition $\theta_{\text{flow}} > 20^\circ$. Square symbols correspond to the $\theta_{\text{plane}} < 75^\circ$ condition and diamond symbols correspond to the $\theta_{\text{plane}} > 75^\circ$ condition. The presented results were sorted using the condition $Z_{\text{frag}} \geqslant 10$.

From Table I we notice that the EF values for experimental data are very close to the model predictions for toroidal configurations. This observation may be one of the arguments in favor of the formation of a toroidal and/or flat freeze-out configuration created in the Au + Au collisions at 23A MeV.

B. Other observables

In order to get additional evidence to support the hypothesis that toroidal objects are created, the behavior of other observables was investigated. We consider here, for each event separately, (i) standard deviation of fragment mass (σ_A),

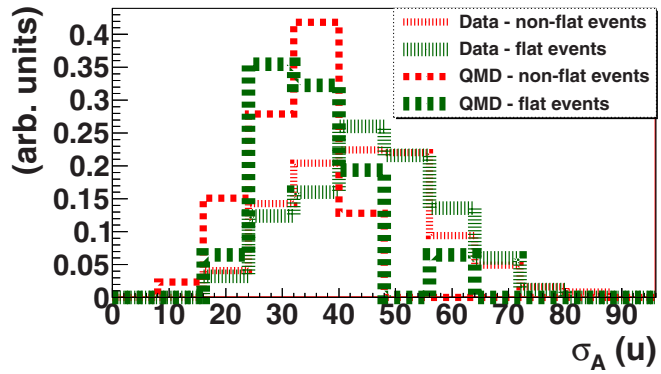

FIG. 13. (Color online) The distributions of standard deviation of the fragment mass for nonflat events (thin red hatched line) and flat events (thick green hatched line) for experimental data and QMD model predictions (thin red and thick green dashed lines, respectively). All the distributions presented here are constructed using the condition $Z_{\text{frag}} \geqslant 10$.

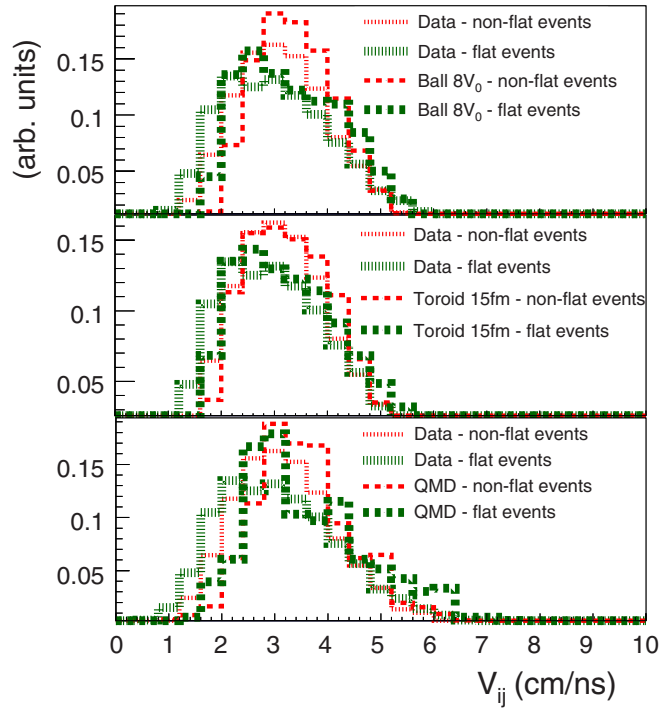

FIG. 14. (Color online) The distribution of relative velocities v_{ij} of fragments pairs for nonflat events (thin red hatched line) and flat events (thick green hatched line) for experimental data compared with Ball 8V_0 (upper panel), Toroid 15 fm (middle panel), and QMD model predictions (bottom panel). All the distributions presented here are constructed using the condition $Z_{\text{frag}} \geqslant 10$.

(ii) relative velocities of fragment pairs (v_{ij}), and (iii) mean velocities of fragments as a function of their mass.

First we construct these observables for events selected by conditions $\theta_{\text{flow}} > 20^\circ$ and $\theta_{\text{plane}} < 75^\circ$, where observation of toroidal freeze-out configurations is expected. The distributions of these observables are generated for flat events selected by condition (7) (thick green hatched line) and nonflat events (thin red hatched line) selected by the conditions

$$\Delta^2 > 0.001c^2 \quad \text{and} \quad \delta > 0.05. \tag{8}$$

TABLE I. The efficiency factor at incident energy 23A MeV for four threshold values of the fragment charge for events selected by conditions $\theta_{\text{flow}} > 20^\circ$ and $\theta_{\text{plane}} < 75^\circ$.

	Efficiency factor (%)			
Configuration	$Z_{\text{frag}} \geqslant 3$	$Z_{\text{frag}} \geqslant 10$	$Z_{\text{frag}} \geqslant 15$	$Z_{\text{frag}} \geqslant 20$
Ball 3V_0	3.3 ± 0.2	3.5 ± 0.2	3.5 ± 0.2	3.5 ± 0.2
Bubble 3V_0	2.4 ± 0.2	2.6 ± 0.2	2.7 ± 0.2	2.7 ± 0.2
Ball 8V_0	3.2 ± 0.2	3.5 ± 0.2	3.5 ± 0.2	3.5 ± 0.2
Bubble 8V_0	3.9 ± 0.2	4.6 ± 0.2	4.7 ± 0.2	4.7 ± 0.2
Toroid 12 fm	29.7 ± 0.6	31.6 ± 0.6	31.8 ± 0.6	31.9 ± 0.6
Toroid 15 fm	25.2 ± 0.5	27.5 ± 0.5	27.7 ± 0.5	27.8 ± 0.5
QMD	13.7 ± 3.4	8.2 ± 4.7	6.3 ± 5.5	N/A
Data	27.1 ± 0.7	26.2 ± 2.5	26.2 ± 4.8	21.1 ± 8.0

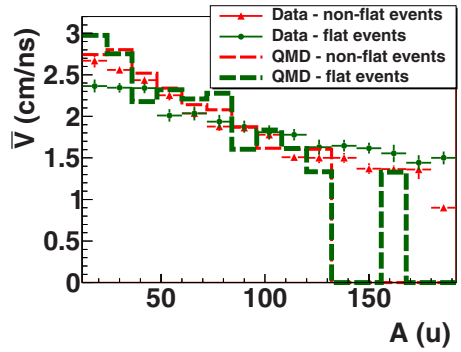

FIG. 15. (Color online) The distributions of mean velocities of fragments as a function of their mass for nonflat events (triangles with error bars) and flat events (points) for experimental data and QMD model predictions (dashed lines). All the distributions presented here are constructed using the condition $Z_{\rm frag} \geqslant 10$

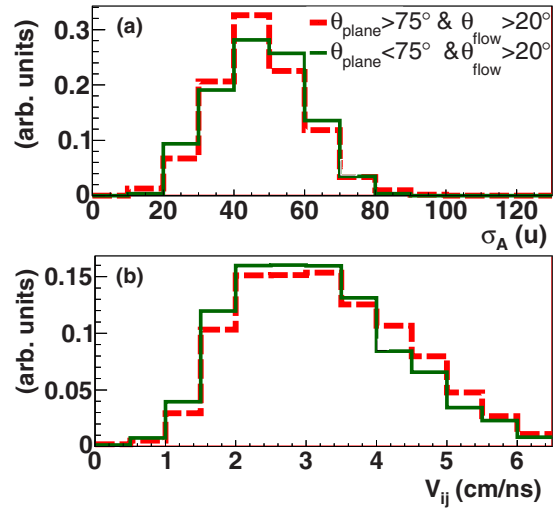

FIG. 16. (Color online) The distributions of standard deviation of the fragment mass (upper panel) and the distributions of relative velocities v_{ij} of fragment pairs (bottom panel) for flat events. The red dashed lines corresponds to events located inside the reaction plane and the green solid lines correspond to events located outside the reaction plane. All the distributions presented here are constructed using the condition $Z_{\rm frag} \geqslant 10$.

Comparison of the σ_A distributions (Fig. 13) for flat and nonflat events indicates that, in the case of flat events, this distribution is slightly shifted to larger values. This observation is in contrast with the expectation that, for the flat events, the enhanced similarity in the size of fragments should be visible. The corresponding distributions for QMD calculations are similar (dashed lines). Their centroids are shifted to smaller values with respect to experimental data.

In Fig. 14 one observes that the distribution of relative velocities for flat events is shifted to smaller velocities with respect to nonflat events. The corresponding distributions for Toroid 15 fm, Ball $8V_0$, and QMD model predictions show a similar dependence. This observation may indicate that the behavior of these v_{ij} distributions is insensitive to the shape of the freeze-out configuration.

In Fig. 15 the distributions of mean velocities of fragments as a function of their mass for flat and nonflat events are presented. On can observe that for flat events velocities of fragments decrease more weakly with mass compared to the same dependence for nonflat events. Comparison with same dependences presented for Pb + Ag and Pb + Au systems at 29A MeV [32] indicates that toroidal configurations may by created for some subclass of flat events.

Properties of flat events in the region where observation of toroidal freeze-out configurations is expected ($\theta_{\rm flow} > 20^\circ$ and $\theta_{\rm plane} < 75^\circ$) can be also compared with properties of flat events corresponding to other regions of $\theta_{\rm flow}$ and $\theta_{\rm plane}$ angles. Here the considered regions are the same as those presented in Fig. 12. The distributions for σ_A of fragments and for v_{ij} of fragment pairs are presented in Fig. 16 using the condition $Z_{\rm frag} \geqslant 10$. The mean values of these distributions are listed in Table II. We note that the corresponding mean values of the distribution of σ_A are similar for all $\theta_{\rm flow}$ and $\theta_{\rm plane}$ windows for a given threshold value of the fragment charge $Z_{\rm frag}$. Such an observation shows us that information carried by σ_A cannot be used as an indication of toroidal object formation. For v_{ij} distributions one observes that the mean values for the class of events located outside the reaction plane are smaller in comparison to the case of events located in the reaction

TABLE II. The mean values of mass standard deviation of the fragments and of relative velocities v_{ij} of fragment pairs for flat events located in different windows of $\theta_{\rm flow}$ and $\theta_{\rm plane}$ angles.

Observable	Threshold	$\theta_{\rm flow} > 20^\circ$ $\theta_{\rm plane} < 75^\circ$	$\theta_{\rm flow} > 20^\circ$ $\theta_{\rm plane} > 75^\circ$	$\theta_{\rm flow} < 20^\circ$ $\theta_{\rm plane} < 75^\circ$	$\theta_{\rm flow} < 20^\circ$ $\theta_{\rm plane} > 75^\circ$
σ_A (a.m.u.)	$Z_{\rm frag} \geqslant 3$	72.09 ± 0.47	71.09 ± 0.35	76.43 ± 0.52	73.33 ± 0.13
	$Z_{\rm frag} \geqslant 10$	47.01 ± 1.88	47.15 ± 1.33	46.41 ± 2.68	45.06 ± 0.58
	$Z_{\rm frag} \geqslant 15$	38.31 ± 2.98	38.53 ± 1.24	35.24 ± 5.11	35.58 ± 0.98
	$Z_{\rm frag} \geqslant 20$	31.01 ± 6.68	31.10 ± 2.60	25.15 ± 5.15	27.17 ± 1.59
	$Z_{\rm frag} \geqslant 25$	17.51 ± 5.07	18.95 ± 5.86	20.94 ± 4.82	18.50 ± 2.23
v_{ij} (cm/ns)	$Z_{\rm frag} \geqslant 3$	3.01 ± 0.01	3.17 ± 0.01	3.27 ± 0.02	3.36 ± 0.01
	$Z_{\rm frag} \geqslant 10$	3.13 ± 0.05	3.30 ± 0.03	3.30 ± 0.08	3.51 ± 0.02
	$Z_{\rm frag} \geqslant 15$	3.16 ± 0.08	3.27 ± 0.05	3.27 ± 0.15	3.49 ± 0.04
	$Z_{\rm frag} \geqslant 20$	3.14 ± 0.24	3.25 ± 0.11	3.24 ± 0.52	3.50 ± 0.06
	$Z_{\rm frag} \geqslant 25$	2.98 ± 0.31	3.28 ± 0.33	3.26 ± 0.81	3.46 ± 0.13

plane. The smallest mean values are seen for the region where observation of toroidal freeze-out configurations is expected. This observation may be used as an indication that, for events located outside the reaction plane, the freeze-out configuration is more extended in comparison with that for events located inside the reaction plane.

Results obtained for the considered observables suggest that the formation of toroidal configurations can be related to a fraction of flat events tilted with respect to the reaction plane ($\theta_{\text{plane}} < 75^{\circ}$). The probability for these events is much greater than the prediction of the QMD model. The nature of these events should be investigated.

Assuming that the total number of detected events corresponds to 80% of the total reaction cross section, the cross section related to the creation of flat tilted events located in the region where observation of toroidal freeze-out configurations is expected can be estimated to be equal to 17 μb.

V. SUMMARY

We presented an analysis of events produced in Au + Au collisions at 23A MeV. Basic information about the data calibration procedure was summarized. The bulk properties of the experimental data were shown. The experimental data were compared with ETNA and QMD model predictions. The proximity of efficiency factor values for experimental data and toroidal freeze-out configurations may be used as an indication of the formation of an exotic freeze-out configuration. The juxtaposition of the standard deviation of fragment mass values for events located outside and inside the reaction plane are not suggestive of a toroidal freeze-out configuration. Comparison of distributions of relative velocities for events with different orientations with respect to the reaction plane gives evidence that the freeze-out configuration is more extended for events located outside the reaction plane. The behavior of mean velocities of fragments as a function of their mass for flat and non-flat events gives an indication that a toroidal configuration may be created for some subclass of flat events.

The probability of the appearence of these flat events is much greater than the prediction of the QMD model. The nature of flat events tilted with respect to the reaction plane should be investigated.

ACKNOWLEDGMENTS

Special thanks are due the INFN-LNS operating crew for providing an excellent beam. This work has been partly supported by the National Science Centre of Poland (Grants No. N N202 180638 and No. 2013/09/N/ST2/04383).

[1] J. A. Wheeler, Nucleonic Notebook, (1950) (unpublished).
[2] P. J. Siemens and H. Bethe, Phys. Rev. Lett. **18**, 704 (1967).
[3] C. Y. Wong, Phys. Rev. Lett. **55**, 1973 (1985).
[4] L. G. Moretto, K. Tso, and G. J. Wozniak, Phys. Rev. Lett. **78**, 824 (1997).
[5] K. Dietrich and K. Pomorski, Phys. Rev. Lett. **80**, 37 (1998).
[6] J. F. Berger *et al.*, Nucl. Phys. A **685**, 1 (2001).
[7] J. Decharge *et al.*, Nucl. Phys. A **716**, 55 (2003).
[8] M. Warda, Int. J. Mod. Phys. E **16**, 452 (2007).
[9] A. Staszczak and C. Y. Wong, Acta Phys. Pol. B **40**, 753 (2009).
[10] A. Sochocka *et al.*, Int. J. Mod. Phys. E **17**, 190 (2008).
[11] A. Sochocka *et al.*, Acta Phys. Pol. B **39**, 405 (2008).
[12] J. Tian, X. Wu, K. Zhao, Y. Zhang, and Z. Li, Phys. Rev. C **77**, 064603 (2008).
[13] K.-L. Pan *et al.*, Phys. Rev. E **80**, 036301 (2009).
[14] A. Pagano, Nucl. Phys. News **22**, 25 (2012), and references therein.
[15] E. De Filippo and A. Pagano, Eur. Phys. J. A **50**, 32 (2014).
[16] A. Sochocka *et al.*, Acta Phys. Pol. B **40**, 747 (2009).
[17] A. Sochocka, Ph.D. thesis, Jagiellonian University, Krakow, 2009 (unpublished).
[18] I. Skwira-Chalot *et al.*, Phys. Rev. Lett. **101**, 262701 (2008).
[19] J. Wilczyński *et al.*, Phys. Rev. C **81**, 024605 (2010).
[20] J. Wilczyński *et al.*, Phys. Rev. C **81**, 067604 (2010).
[21] T. Cap *et al.*, Phys. Scr. **89**, 054005 (2014).
[22] G. Tăbăcaru *et al.*, Nucl. Instrum. Methods A **428**, 379 (1999).
[23] G. Pasquali *et al.*, Nucl. Instrum. Methods A **405**, 39 (1998).
[24] K. Sümmerer *et al.*, Phys. Rev. C **42**, 2546 (1990).
[25] K. Sümmerer and B. Blank, Phys. Rev. C **61**, 034607 (2000).
[26] K. Sümmerer, Phys. Rev. C **86**, 014601 (2012).
[27] G. Lanzalone, INFN Laboratori Nazionali del Sud, LNS Activity Report (2004), p. 125 (unpublished).
[28] T. Cap *et al.*, Phys. Scr. **T154**, 014007 (2013).
[29] J. Aichelin, Phys. Rep. **202**, 233 (1991).
[30] J. Lukasik and Z. Majka, Acta Phys. Pol. B **24**, 1959 (1993).
[31] J. Cugnon and D. L'Hote, Nucl. Phys. A **397**, 519 (1983).
[32] B. Jouault *et al.*, Nucl. Phys. A **615**, 82 (1997).